Chapter 6

Spinning "Free" Disc Flow

6.1 Introduction

There have been numerous studies of the flow induced by a spinning disc in an infinite quiescent environment, or free-disc flow. The case represents one of the simplest wall-bounded flows involving strong rotational forces. By far the greatest interest in spinning discs comes from simulations of flow through gas turbines, where it is common practice to first validate a CFD code with the free-disc flow, before moving on to study more complex enclosed disc flows which occur inside the turbine. Other practical examples of spinning-disc flows include computer hard disks and wheels on moving vehicles. Experimental studies have shown that approximately one third of the total drag on a typical saloon car is due to the interaction between the flow around the spinning wheels and their associated structures [111], so clearly one would like to predict accurately the flow around the spinning wheel.

In a free-disc flow, the disc of radius r_b rotates with angular velocity Ω and, due to the no-slip condition on the surface of the spinning disc, a tangential velocity $(W = \Omega r)$ is imparted to the fluid in contact with the disc. A radial outflow of fluid from the centre of the disc is also induced due to the centrifugal force. The entrainment of fluid axially into the boundary layer and the exit of the fluid radially is referred to as the "free-disc entrainment rate" or "free-disc pumping effect" [112]. When the disc is spinning sufficiently fast, the boundary layer can become turbulent. The location of transition from laminar to turbulent flow depends upon the local rotational Reynolds number (based on the tangential velocity of the disc and the radius from the disc axis), the surface roughness of the disc and external disturbances to the fluid flow. Experimental studies of the free-disc flow have reported a certain degree of variation in the location of this transition. Gregory *et al.* [113], reported that the transition started at a rotational Reynolds number of approximately $185,000$ which led to fully-developed turbulence at $Re_\phi = 285,000$, whilst Theodorsen & Regier [114] found that transition started at around $Re_\phi = 310,000$ for a highly polished disc and $Re_\phi = 220,000$ for a rough disc. Owen *et al.* [115] even found no sign of transition at all, which was attributed to a 2 degree taper on the disc faces and the presence of a central driving shaft. Once the boundary layer has become fully turbulent, the tangential velocity exhibits a logarithmic velocity profile near the wall whilst the radial velocity

increases from zero at the wall to a peak and then decays with distance from the disc [116].

Mayle [117] describes three modes in which transition occurs from laminar to turbulent flow: natural, bypass and separated-flow transition. In free-disc flows, transition occurs in the "natural" mode, in which a weak instability in the laminar boundary layer leads to the formation of two-dimensional Tollmien-Schlichting waves which are amplified to form hairpin vortices and turbulent spots that grow and are convected downstream until eventually they coalesce to form a fully-turbulent boundary layer. Schlichting [118] noted that the transition mechanism in the free-disc boundary layer is slightly different to that exhibited by classical 2-*D* flat-plate flows. In particular, stationary spiral vortices are formed on the free-disc which show some similarity to Taylor-Görtler vortices [119]. In "bypass" transition, a relatively high free-stream turbulence level diffuses turbulent kinetic energy into the laminar boundary layer. Turbulent spots can appear directly without the preceding stages of T-S waves found in natural transition. In gas turbines, transition on the surface of turbine discs occurs primarily in the bypass mode, while the flow of air over the car wheel is arguably fully turbulent. Although the free-disc flow serves as a useful test-case for validating turbulence models and near-wall treatments for eventual application to gas-turbine flows, or flows around moving vehicle wheels, the mechanism of transition in these cases is different. Therefore, the prediction of transition in the free-disc flow should in many respects be looked at as a separate issue to that of transition prediction in gas turbines or car wheels.

Although the flow is geometrically simple, there are several challenges for the numerical simulation of turbulent free-disc flows using Reynolds-averaged Navier-Stokes equations. Firstly, as already indicated, the flow involves transition from laminar to turbulent flow. This is notoriously difficult to locate accurately and repeatably, and is highly sensitive to the turbulence model, the numerical scheme and the initial turbulence levels [120]. Secondly, the large near-wall cells commonly used with high-Reynolds-number models and wall functions cover the region of the flow where there is a peak in the radial velocity profile. Capturing this type of velocity variation presents an impossible problem for wall functions based on the log-law velocity profile. Moreover, it is usually recommended that, if a wall-function approach is adopted, the near-wall node should be located at a dimensionless wall distance, $y^+ = yU_\tau/\nu$, between 30 and 100 [121]. Since the friction velocity, U_τ, increases with radial distance one may be forced to adopt a non-orthogonal grid to maintain the y^+ value at the near-wall node between these limits. In addition, wall functions are typically developed with reference to simple channel flows in which there is only one Reynolds shear stress, $\overline{uv}$. In the spinning-disc flow, one needs to also account for the $\overline{uw}$ and $\overline{vw}$ shear stresses.

Whilst the free-disc flow is a challenging computational test-case, in terms of predicting transition from laminar to turbulent flow and applying a wall treatment that can capture the near-wall skewing of the velocity profile, quite acceptable results can be achieved using a fairly simple mixing-length turbulence model and a parabolic solver (e.g. Owen *et al*. [115]). Moreover, this method would be considerably faster than the linear and non-linear two-equation models and the elliptic solver used in the present study. However, one would clearly like to have a generally applicable computational

method that can be applied to a wide variety of flows without the need for significant re-optimization. Whilst a mixing-length turbulence model with a parabolic solver may be adequate for the free-disc flow it would be inappropriate for the study of flow around a car body, for example, or even the impinging jet flow considered in Chapter 5.

6.2 Previous Experimental and Computational Studies

There have been numerous computational studies of the turbulent spinning free-disc flow. Owen & Wilson [112] reviewed a number of solutions of the momentum-integral boundary-layer equations using assumed velocity profiles and empirical correlations. Accurate heat transfer predictions of the free-disc have been made using parabolic finite-difference solvers with both mixing-length and two-equation turbulence models (e.g. Owen *et al*. [115] and Launder & Sharma [13], respectively). However, there have been relatively few studies of free-disc flows using high-*Re* turbulence models with wall functions. Chew [122] used the elliptic TEACH code with the high-*Re* $k-\varepsilon$ model previously used by Gosman *et al.* [123] and studied the flow between co-rotating discs, a rotor-stator cavity and the free-disc. The predicted tangential wall shear stress in the free-disc flow was in poor agreement with both experiment and previous integral-momentum solutions. Predictions of the flow between rotating and stationary discs also showed relatively poor agreement with both the experimental radial velocity distribution and the earlier work of Gosman *et al.*, which had shown more encouraging results. It was suggested that the differences with the previous numerical study were due to an insufficient grid density being used by Gosman *et al.*, which was shown to have a significant effect on the moment coefficient. In the third flow considered by Chew, that between co-rotating discs, it was found that the low-*Re* model of Launder & Sharma tended to laminarize much of the cavity which experimentally had been turbulent. This final result was confirmed by Morse [124] in a subsequent study of turbulent flow in rotating cavities. Williams *et al.* [125] studied enclosed spinning-disc flows using a high-*Re* $k-\varepsilon$ model with simple wall functions and the Lam & Bremhorst low-*Re* $k-\varepsilon$ model. The wall-function model outperformed the low-*Re* model in predicting both tangential and radial velocity profiles and the authors concluded that the wall-function approach was to be preferred since it was far more economical in computing time. Virr *et al.* [121] also studied the flow in rotating cavities using the Launder & Spalding $k-\varepsilon$ model with both wall functions and a two-layer near-wall one-equation model. They reported that the wall function returned acceptable results provided that the boundary layer was fully turbulent and that the y^+ was maintained between 30 and 100. A comprehensive comparison of different turbulence models and near-wall treatments for rotating flows was given by Owen & Wilson [112]. They concluded that “at present only low-Reynolds-number $k-\varepsilon$ models have been shown to give good predictions of both flow and heat transfer over the complete range of test cases”.

A number of studies have alluded to convergence difficulties with the free-disc flow. Chew [122] found that, using a high-*Re* model with wall functions, axial grid-refinement led to instability problems. This may have been due to more of the near-wall cells occupying the viscous sublayer region in

which case the wall functions resorted to laminar-type boundary conditions. Chew also encountered problems with the low-*Re* Launder & Sharma model where there was a tendency for the boundary layer to laminarize. In the original calculations by Launder & Sharma [13], transition was triggered by an injection of turbulence energy at a specified radial location. Morse [126] and Ong [127] also reported difficulties in predicting the onset of transition with low-*Re* $k-\varepsilon$ models. To achieve transition, Morse resorted to modifying the eddy-viscosity in the turbulent kinetic energy production term with a proportion of the eddy-viscosity calculated by a mixing-length model. Ong used the Launder & Sharma model with a parabolic semi-implicit Keller-box method and found that if the calculation was started in the laminar boundary-layer region of the free-disc, the solution would remain laminar and never undergo transition to turbulence. To obtain results for the turbulent boundary layer, Ong started the calculation at a radial position corresponding to $Re_\phi = 600,000$, although it was reported that even starting from what should be a fully-developed turbulent region, the boundary layer thickness showed a tendency to decay and laminarize. In contrast to these earlier calculations, Kiliç [128] did not report any difficulties in predicting transition with the same turbulence models using a two-dimensional, elliptic, multigrid solver. Kiliç found that transition occurred naturally at $Re_\phi \approx 150,000$. In the present study, the flow field was initialized with a uniform turbulence level and, as the calculation progressed, turbulence decayed near the axis of the disc to form a laminar boundary layer whilst at a greater radial distance the flow remained fully turbulent. No attempts were made to artificially induce transition and it was found that transition occurred naturally at approximately the same location as Kiliç found (see later discussion).

6.3 Computational Details

6.3.1 Models Used

Two low-Reynolds-number models were tested in the free-disc flow: the Launder & Sharma $k-\varepsilon$ model [13] and the non-linear $k-\varepsilon$ model of Craft *et al.* [30, 67]. Results obtained using the low-*Re* models were compared to those obtained using three "standard" wall functions: Launder & Spalding (TEAM), simplified Chieng & Launder (SCL) and Chieng & Launder (CL) and the new wall function, UMIST-*N*. The standard wall functions all employed a logarithmic profile for both the radial and tangential velocity if the near-wall node was at a dimensionless wall distance of $y^+ \geq 11.6$. If the near-wall node was within the viscous sublayer $(y^+ < 11.6)$ a linear profile was adopted (for details see Chapter 2). The same turbulence model was applied across the subgrid domain of the UMIST-*N* wall function as across the main-grid domain.

6.3.2 Numerical Methods

The free-disc flow was examined using the TEAM code, described in Section 3.2. Diffusion terms appearing in the transport equations were approximated using central differencing. Convective terms

in the momentum and temperature equations adopted the third-order QUICK scheme whilst the power-law differencing scheme, PLDS, was used for turbulence parameters. It was found that the unbounded QUICK scheme led to instability in the initial stages of the calculations and therefore PLDS was used for all quantities in the first 500 or so iterations (approximately $10-25\%$ of the full calculation length of the wall-function calculations). In addition, with the wall-function calculations, PLDS was always used for the wall-adjacent cells. The quadratic interpolation used by QUICK employs two upstream nodes which, if the flow was directed away from the wall, would involve the node on the wall and the wall adjacent node. Since there are abrupt changes in the velocity within the large near-wall cell used with a wall-function approach, the use of these two nodal values could produce unrealistic interpolated velocity profiles which was found to lead to numerical instability (particularly with large near-wall cells). The use of PLDS within the near-wall cells was not considered to be too restrictive on numerical accuracy since one would expect the near-wall flow to be parallel to the wall, in which case PLDS and QUICK would give similar results.

Residuals were summed across all the nodes in the flow domain and non-dimensionalized with a characteristic value for the particular variable. For the momentum equations this was the momentum flux defined using the velocity at the edge of the disc (Ωr_b). The turbulent kinetic energy residual was non-dimensionalized with the flux defined using the velocity scale $(\Omega r_b)^2$, whilst the dissipation rate, ε, was non-dimensionalized using the kinetic energy flux and an assumed length scale $l = r_b$. A mass imbalance was calculated rather than a pressure residual which was also non-dimensionalized using (Ωr_b). Unlike previous studies [124, 128] the factors used to non-dimensionalize the residuals were not linked to the mass flow rate since this varied considerably during the calculation. As a consequence, during a calculation from an initially quiescent flow-field, residuals increased and then decayed. The calculation was stopped when momentum and turbulent kinetic energy residuals fell below 10^{-7}. All the residuals decreased by at least 3 orders of magnitude from their maximum values. It was verified that using more stringent convergence criteria had no effect on results.

Under-relaxation factors were set at a relatively low level for all the calculations performed in the present work, as shown in Table 6.1. Subgrid under-relaxation factors used for the free-disc flow are given in Table 6.2. Previous tests with the UMIST-*N* wall function in the impinging jet found that the under-relaxation of the subgrid turbulence parameters needed to be increased as the size of the near-wall main-grid cell (and hence the number of subgrid nodes) was increased. In the present work, the under-relaxation factors given in Table 6.2 were used throughout.

U	V	W	P	k	ε	T	NL
0.2	0.2	0.2	0.3	0.1	0.1	0.4	0.5

Table 6.1: Under-relaxation factors used for the free-disc flow with low-Reynolds-number models, standard wall-function calculations and in the main-grid with UMIST-*N* wall function calculations (*NL* refers to the Non-Linear EVM terms).

U	W	k	$\tilde{\varepsilon}$	T	NL
1.0	1.0	0.9	0.9	1.0	1.0

Table 6.2: Subgrid under-relaxation factors for the free-disc flow used with the linear and non-linear $k-\varepsilon$ models

6.3.3 Domain and Grid

Figure 6.1 shows the domain size and boundary conditions used for the free-disc study. Following Kiliç [128], a domain height of $0.06D$ was used which corresponds to three times the boundary layer thickness at the outside edge of the disc, where $Re_\phi = 3.3 \times 10^6$, as determined from von Kármán's correlation for turbulent flow over a free-disc [129].

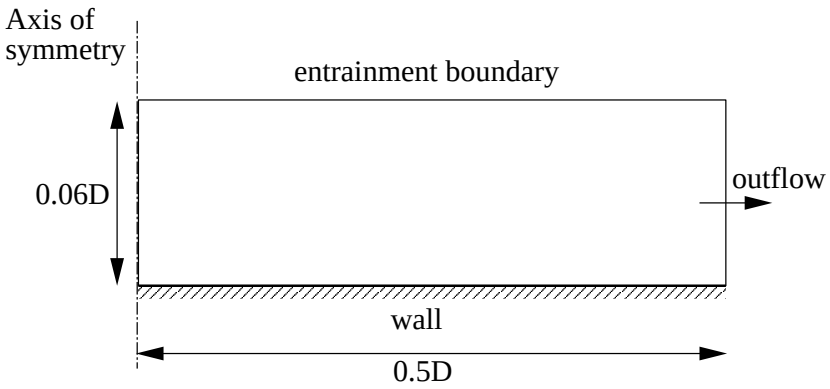

Figure 6.1: Free-disc boundary conditions

A number of previous spinning-disc studies have noted that the placement of grid nodes near the wall is important in obtaining reliable wall shear stress and moment coefficient predictions [112, 128]. Using the same domain size and Reynolds number, Kiliç [128], previously used a low-*Re* grid of 67×67 nodes and checked grid-dependence using a 91×115 (axial $\times$ radial) grid. In the present study, in order to ensure that adequately grid-independent low-*Re* results were obtained, grid refinement was studied separately in the radial and axial directions.

Radial Grid-Refinement

Three different grid densities were tested in the radial direction with 90, 120 and 150 nodes, using 70 nodes in the axial direction (see Figures 6.2, 6.3 and 6.4). Figure 6.5 shows the predicted Nusselt number from these three grid arrangements. The location of transition shifts slightly downstream as one moves to the higher grid density, with approximately the same difference from the 90×70 to the 120×70 grid as from the 120×70 to the 150×70 grid. Clearly the logarithmic plot magnifies the differences in the transition region and, as shown by Figure 6.6, the shift in the transition location achieved by increasing the number of radial nodes by 30% is equivalent to the distance between two or

perhaps three nodes. Following this study, 120 nodes were used in the radial direction for all low-*Re* and wall-function calculations.

Axial Grid-Refinement

Axial refinement of the low-*Re* grid was achieved by increasing the number of nodes from 70 to 120, using 120 nodes in the radial direction in both cases (Figures 6.3 and 6.7). Predicted Nusselt number using the low-*Re* Launder & Sharma $k-\varepsilon$ model are shown in Figures 6.8*a* and 6.8*b*, on semi-logarithmic and linear axes respectively. Corresponding y^+ values for the near-wall node and for the first 10 near-wall nodes are shown in Figures 6.9*a* and 6.9*b*. In order to obtain $y^+ < 0.8$ for the 120×70 grid, an expansion ratio of 1.15 was required for the near-wall cells. The 70 percent increase in the number of nodes in the axial direction shows negligible difference in the predicted Nusselt number on semi-log axes (Figure 6.8*a*), although closer inspection of the Nusselt number distribution on linear axes (Figure 6.8b) shows a maximum difference of just under 2% which occurred at the outside edge of the disc. The use of 70 nodes in the axial direction was therefore considered adequately grid-independent[1].

Four high-Reynolds-number grids were used in the present study to assess the sensitivity of the standard and UMIST-*N* wall functions to changes in the width of the near-wall cell, over which the wall function was applied. In order to avoid sudden increases in cell sizes from the near-wall cell to the adjoining cell, the number of nodes in the axial direction was varied from 22 to 30 (shown in Figures 6.10 to 6.13). With 22 axial cells there was no clustering of cells (i.e. the axial width of the grid cells was constant across the whole flow domain) whilst, with a larger number of radial nodes, there was a small degree of clustering towards the wall. The wall-adjacent cells in the low-*Re* calculations had an average aspect ratio of approximately $2900:1$ whilst the wall-function grid with 28 axial cells cells had an aspect ratio of approximately $5:1$.

The number of subgrid cells used within the wall-adjacent main-grid cell was adjusted for each high-*Re* mesh to ensure that grid-independent results were obtained. Figure 6.14 shows the predicted Nusselt number using the 28×120 high-*Re* mesh with between 30 and 50 subgrid nodes. The expansion ratio used to generate the subgrid mesh was also modified in each case to maintain the size of the wall-adjacent subgrid cell such that $y^+ < 1$ (expansion ratios are shown in parentheses in the key of Figure 6.14). Figure 6.14 shows that there was negligible difference in the predicted Nusselt number due to an increase the number of subgrid nodes from 30 to 50. The total number of subgrid plus main-grid nodes (i.e. 30×120 subgrid and 28×120 main-grid nodes) was thus slightly less than that required by low-Reynolds-number models (70×120 nodes).

[1] Interestingly, the physical width of the wall-adjacent cell with the 70×120 grid is $1.6 \times 10^{-6} D$, where D is the diameter of the disc (the node within this cell has a maximum $y^+ = 0.64$ at the edge of the disc). Using the same rotational speed and viscosity as Cobb & Saunder's experiments [130] (which had an 18-inch disc for a Reynolds number of up to 0.8×10^6), the width of the near-wall cell in the current tests corresponds to 1.5×10^{-6}metres. By comparison, the minimum value of the Kolmogorov microscale $\eta = \left(\nu^3/\varepsilon\right)^{1/4}$, based on the value of ε at the near-wall node at a rotational Reynolds number, $Re_\phi = 3 \times 10^6$, was of the order $\eta = O\left(10^{-4}\right)$ metres.

6.3.4 Boundary Conditions

A schematic of the boundary conditions for the free-disc flow is shown in Figure 6.1.

Axis of Symmetry

The radial (U) and tangential (W) velocity were set to zero on the boundary nodes (in both the main grid and the subgrid) and zero gradient conditions were applied for the wall-normal (axial) velocity, V, turbulent kinetic energy, k, dissipation rate, ε, and temperature, T.

Entrainment Boundary

For the entrainment boundary condition at the northern edge of the flow domain, shown in Figure 6.1, different constraints were applied depending upon the local flow direction. If the flow was entering the domain, k and ε were given small but finite values[2], the radial and tangential velocity were set to zero and the temperature of the flow entering the domain was set to the "ambient" temperature (defined as $T_{amb} = 0$ in the present work). If fluid was leaving through the entrainment boundary then zero-gradient conditions were applied for U, W, k, ε and T. Irrespective of the flow direction, the pressure at the node just inside the entrainment boundary was set to zero and the axial velocity on the boundary of the domain, V_N, was set equal to the neighbouring nodal value.

Circumferential Exit Plane

Although in theory the flow through the east face of the domain should be leaving the domain, during the iteration process flow may enter or leave through the boundary. For this reason the entrainment conditions described above were also used for the circumferential exit plane. The only difference here was that the radial velocity specified on the boundary was determined from:

$$\frac{\partial (rU)}{\partial r} = 0 \tag{6.1}$$

This condition is used so that continuity is satisfied within the cells adjacent to the exit plane.

6.3.5 Initial Turbulence Levels

In order to obtain turbulent flow predictions for the spinning free-disc in a quiescent atmosphere, in which the ambient turbulence levels are practically zero, one must start the calculation from an initially turbulent flow field. If the flow field is initialized with zero turbulence levels then, since turbulence energy does not enter the flow domain through the boundaries of the domain, the flow will remain laminar no matter how high the rotational Reynolds number. Clearly one would like to obtain results that are independent of the chosen initial turbulence levels i.e. one should not obtain a multitude of

[2]Incoming flow turbulence levels were $k = 0.01V_N^2$ and $\varepsilon = \rho c_\mu (k^*)^2 / (0.01\mu)$, where V_N is the axial velocity through the boundary.

fully-converged solutions depending upon the point from which the calculation was started. However, in the present study it was found that the location of the transition from laminar to turbulent flow over the free-disc (or its disappearance altogether) can indeed be affected by the initial turbulence field used in the numerical simulation unless certain precautions are taken. Using these simple precautions, the same location of transition can be calculated, independent of the turbulence initialization.

Morse [126], studied the flow over a spinning disc using two low-Reynolds-number $k-\varepsilon$ models with a parabolic solver and found that an *ad hoc* artificial turbulence viscosity input was required to prevent laminarization of the boundary layer. Morse commented that this was necessary since "it is difficult to effect the transition to turbulent flow with the computation started from reasonable levels of turbulent kinetic energy". Owen & Wilson [112] also mention briefly that the performance of the Morse model and the Launder & Sharma model is sensitive to the initial turbulence field. Kiliç [128] studied the spinning disc flow using the same turbulence models as Morse, with a multigrid solver (in which the turbulence parameters were only solved on the finest mesh) adopting the following initial turbulence levels[3]:

$$k = 10^{-6}\,(\Omega r)^2 \tag{6.2}$$

$$\mu_t = 0.09\mu \tag{6.3}$$

$$\varepsilon = 0.01\rho\frac{k^2}{\mu} \tag{6.4}$$

In contrast to the earlier studies, Kiliç reported that this initial turbulence field was sufficient to cause transition without the need for an artificial production of kinetic energy input.

The following sections describe the initialization of the dynamic field used with low-Reynolds-number models, standard wall functions and the UMIST-*N* wall function.

Low-Reynolds-Number Model

Tests with the low-Reynolds-number models showed that with different starting conditions for k and ε (or μ_t) not only could the flow revert fully to laminar, but that the radial location of transition could be shifted according to the initial turbulence levels chosen. Furthermore, an increase in the under-relaxation moved the transition point to higher rotational Reynolds numbers (i.e. radially outward), particularly for lower initial values of k and μ_t. Table 6.3 shows a matrix with different initial conditions for k on the x-axis and different initial conditions for μ_t on the y-axis. The cells in the table indicate whether the calculation was stable starting from the specified turbulence levels, and if so, a description of the flow: whether the boundary layer was completely laminar or, if transition from laminar to turbulent flow occurred, its location given by the rotational Reynolds number $\left(Re_\phi = \Omega r^2/\nu\right)$. Initial ε values for each entry can be calculated from $\varepsilon = \rho c_\mu k^2/\mu_t$. The calculations described in the Table 6.3 were all obtained using the Launder & Sharma $k-\varepsilon$ model with power-law

[3]There may be an internal inconsistency in Kiliç's values, since typically one would set the levels of two of the variables: k, μ_t and ε, and obtain the third parameter from the definition of the eddy-viscosity, $\mu_t = \rho c_\mu k^2/\varepsilon$. If one accepts the value Kiliç quotes for ε and takes the value of $c_\mu = 0.09$, the initial eddy-viscosity would be $\mu_t = 9\mu$.

differencing (PLDS [74]) for the convective fluxes of momentum and turbulence parameters, and the under-relaxation factors[4] given in Table 6.1.

	$k = 10^{-5}(\Omega r_b)^2$	$k = 10^{-4}(\Omega r_b)^2$	$k = 10^{-3}(\Omega r_b)^2$
$\mu_t = 10\mu$	marginally stable laminar	stable $Re_\phi \approx 4.8 \times 10^5$	stable $Re_\phi \approx 1.0 \times 10^6$
$\mu_t = 100\mu$	marginally stable mostly laminar	stable $Re_\phi \approx 1.3 \times 10^5$	stable $Re_\phi \approx 1.3 \times 10^5$
$\mu_t = 400\mu$	unstable	marginally stable $Re_\phi \approx 1.3 \times 10^5$	stable $Re_\phi \approx 1.3 \times 10^5$

Table 6.3: Predicted transition locations using the low-*Re* Launder & Sharma $k-\varepsilon$ model with different initial turbulence levels

A comparison of the predicted Nusselt number for four of the cases given in Table 6.3 is presented in Figure 6.15. The strong dependence upon the initial turbulence level and the degree of under-relaxation was traced to the initially large magnitude of the near-wall turbulence damping terms and the relatively slow development of the boundary layer with low-*Re* models. In the very first iteration of the numerical simulation, the wall has tangential velocity (Ωr) whilst the neighbouring fluid elements have zero velocity. The large initial near-wall velocity gradient $(\partial W/\partial y)$ led to appreciable damping of the turbulence by the gradient production, $P_{\varepsilon 3}$, in the $\tilde{\varepsilon}$-equation[5]. In cases with low initial turbulence levels, the near-wall turbulence was heavily damped in the initial stages of the calculation and the turbulence level elsewhere had decayed to such an extent that by the time that the boundary layer had developed the whole flow became laminar. If the update of the momentum equations was slowed by increasing the level of under-relaxation, the turbulence had a proportionally greater time to dissipate before the boundary layer developed, and so one saw that the location of transition moved progressively downstream as the level of under-relaxation increased. In contrast to cases of bypass transition, where diffusion of turbulent kinetic energy into the boundary layer from the main flow is responsible for transition, in the free-disc flow the level of turbulence in the surrounding region is zero and so, no matter how long the calculation is run, once the boundary layer has fully laminarized it will never become turbulent[6].

If high initial values of k and μ_t were specified, the turbulence level still decayed as the calculation progressed, but μ_t was sufficiently large by the time that the boundary layer had developed that there

[4]Lower under-relaxation factors were required with $k = 10^{-5}(\Omega r_b)^2$ to obtain converged results ($\alpha_{U,V,W} = 0.1$ and $\alpha_P = 0.2$).

[5]The behaviour of the numerical simulation in the first few iterations is highly complex with large velocity gradients driving both production and destruction terms in the turbulence field. The gradient production term has been singled out here as this term was found to be of particularly large magnitude initially and, as will be discussed with the UMIST-*N* wall function, a temporary switch to remove or clip $P_{\varepsilon 3}$ in the early stages of a calculation was found to lead to a turbulent boundary layer developing with transition in the correct location. This could, however, be attributed to the temporary removal of a turbulence sink, and it may be that a similar outcome could be obtained by reducing other turbulent kinetic energy sink terms.

[6]Once k has fallen to zero, or been clipped to a very small but positive value, the eddy-viscosity, $\mu_t = c_\mu f_\mu k^2/\tilde{\varepsilon}$, is also practically zero, so that no matter how large the strain-rates, the production of turbulent kinetic energy, $P_k = \mu_t S_{ij}\partial U_i/\partial x_j$, is never sufficiently large to increase the turbulence level.

was sufficient production of kinetic energy to sustain the turbulence. The fully turbulent boundary layer then decayed to a laminar boundary layer in regions of low strain-rate, near the axis of the disc. Whilst this approach of specifying a high level of initial turbulence solved the laminarization problem, it was at the expense of the computational time, since one was starting from an initially unrealistic turbulence field.

The alternative to specifying a high initial turbulence field to correctly capture transition was to initialize the dynamic field so that the boundary layer had already partially developed before turbulence parameters were evaluated. The near-wall velocity gradient was then of more moderate magnitude, so that the initial values of the near-wall turbulence damping terms were reasonable. The boundary layer also extended further into the flow domain, so that production of turbulent kinetic energy was not restricted to such a thin layer adjacent to the wall. To initialize the dynamic field, the momentum and pressure-correction equations were solved with frozen μ_t for the first 1000 iterations (approximately 5% of the total number of iterations required for the calculation to converge) before calculation of k and $\tilde{\varepsilon}$ commenced. Using initial turbulence levels of $k = 10^{-5}(\Omega r_b)^2$ and $\mu_t = 10\mu$, which had previously led to a totally laminar boundary layer (see Table 6.3 and Figure 6.15), transition was predicted at precisely the location previously obtained when a much greater initial level of turbulence was specified $\left(Re_\phi \approx 1.3 \times 10^5\right)$. In fact, by initializing the dynamic field using a frozen μ_t before starting to solve for k and $\tilde{\varepsilon}$, the same transition location was predicted, independent of the initial turbulence level or the degree of under-relaxation. This, perhaps, explains the previous findings of Kiliç [128] who studied the spinning disc flow using a multigrid solver, in which the turbulence parameters were only solved on the finest grid. Kiliç did not report any problems obtaining transition to turbulence, unlike previous authors. In effect, the multigrid method initialized the dynamic field before starting to solve for the turbulence parameters.

"Standard" Wall Functions

The simplified Chieng & Launder (SCL) and the Chieng & Launder (CL) wall functions both predicted transition whilst the TEAM wall function treated the boundary layer as fully-turbulent across the whole of the disc. The location of transition with the SCL and CL wall functions was shifted according to the initial turbulence levels specified. Figure 6.16 shows Nusselt number predictions from using two different initial turbulence levels for the SCL and CL wall functions respectively. The initial turbulent kinetic energy level in all cases was $k = 10^{-5}(\Omega r_b)^2$ with the solid lines representing an initial eddy-viscosity $\mu_t = 10\mu$ and dashed lines $\mu_t = 400\mu$.

Figure 6.16 shows that different initialization of the flow field can lead to different predicted transition locations. There are also "spikes" in the Nusselt number predictions with both wall functions near to transition. These spikes were due to the switch within the wall functions which stated that if $y^+ > 11.6$ at the near-wall node, turbulent boundary conditions applied, otherwise the flow was assumed to be laminar. Figure 6.17 shows that changing the level of under-relaxation has a small but measurable effect on the predicted Nusselt number when using the Chieng & Launder wall function.

The approach described above for low-*Re* model calculations to obtain results independent of initial turbulence levels is unlikely to work with standard wall functions. The problems with low-*Re* models are related to the over-damping of turbulence in the initial stages of a calculation when there are very large strain-rates near the wall. Standard wall functions do not include low-Reynolds-number damping terms and hence are not affected in this way. One could investigate using the wall shear stress instead of $k^{1/2}$ as the scaling parameter in the friction velocity, U_τ, used by the wall functions. This may solve the immediate problem of the standard wall functions switching between linear and logarithmic velocity profiles when k falls below a certain level, but in flows involving separation or reattachment the wall shear stress vanishes and one is forced to use $k^{1/2}$ in U_τ.

UMIST-*N* Wall Function

The UMIST-*N* wall function required some attention in order to obtain transition to turbulence that was independent of the specified initial turbulence level. Without any special treatment, solving momentum and turbulence parameters from the start of the calculation, and initializing both the main-grid and the subgrid with a moderate turbulence level (say, $k = 10^{-5}(\Omega r)^2$ and $\mu_t = 10\mu$), the calculation diverged after approximately 100 iterations. The instabilities stemmed from the wall shear stress changing sign, a consequence of the tangential velocity at the near-wall node becoming greater than that at the wall. This was traced to the initial viscosity profile adopted across the subgrid which, during the first few iterations, led to a rapid change in tangential velocity across the wall-adjacent subgrid cell. The large strain-rate across the wall-adjacent subgrid cells led to a very large tangential wall shear stress, $\tau_{wall,\phi}$, and gradient production source term, $P_{\varepsilon 3}$. The overly large $\tau_{wall,\phi}$ caused the main-grid tangential velocity to exceed the wall velocity whilst the subgrid-averaged source term $\overline{P_{\varepsilon 3}}$ was sufficient to suppress the turbulence in the near-wall cell, leading in some cases to laminarization of the boundary layer.

To initialize the subgrid such that predictions were independent of the initial turbulence level, the following steps were taken:

- The main-grid and subgrid velocity fields were initially zero.
- The main-grid and subgrid were initialized with a specified level of turbulence (any of the values given in Table 6.3).
- The value of $\overline{P_{\varepsilon 3}}$ obtained from the first subgrid iteration was set to zero.
- A constant value of μ_t was assumed across all of the subgrid cells (calculated from the initial turbulence level and $\mu_t = \rho c_\mu k^2/\varepsilon$) except for two wall-adjacent subgrid cells in which the subgrid eddy-viscosity was reduced to approximately $\mu_t \approx \mu$ (the solution was insensitive to the actual value, as long as it was in the range $0.5\mu < \mu_t < 3\mu$). This condition was only applied for the first iteration, after which μ_t was calculated from $\mu_t = \rho f_\mu c_\mu k^2/\tilde{\varepsilon}$ as usual[7].

[7]The relation $\mu_t = 0.09k^2/\varepsilon$ did not hold within the two wall-adjacent subgrid cells since initial values for μ_t were

6.3.6 Differential Length-Scale Correction

In tests with the free-disc flow, it was found that the original differential Yap correction developed by Iacovides & Raisee [66], given by Equation (2.17) with constant $c_w = 0.83$, introduced numerical instability arising from a significant turbulent length-scale gradient at the edge of the turbulent boundary layer. This was despite the actual turbulence level being practically zero in this region. Figure 6.18 shows contours of the turbulent length scale gradient $\left(\left|\partial l/\partial x_j\right|\right)$ for the free-disc flow. Near the axis of the disc the flow is laminar; at a radius of approximately $r/D = 0.12$ transition occurs and thereafter one can see in Figure 6.18 the radial growth of the turbulent boundary layer. At the edge of the turbulent boundary layer there are large turbulent length scale gradients related to the difference between the value of the length scale at one node inside the boundary layer and the length scale at the neighbouring node in which the value of k was clipped to a very small but finite value (10^{-15}). Clipping was applied after each successive iteration of the k-equation such that the minimum value of k was 10^{-15}. If this clipping was not applied, small negative values of k could arise during the iteration process, especially in regions where k was naturally very small (i.e. outside the turbulent boundary layer). Additionally, zero values of k introduce singularities into the $\tilde{\varepsilon}$-equation source terms which involve the ratio $\tilde{\varepsilon}/k$. Figure 6.19 shows the magnitude of the differential Yap correction, Y_{dc}, based on the length-scale gradient shown in Figure 6.18. Numerical instability was caused by the significant correction to the $\tilde{\varepsilon}$-equation (with $Y_{dc} \approx 10^7$) at the edge of the turbulent boundary layer.

The Iacovides & Raisee turbulent length scale correction was later modified by Craft *et al.* [67], who introduced a variable c_w term (see Equation 2.20) to reduce the degree of correction in regions of high straining. This correction improved the numerical stability and the resulting Yap correction is shown in Figure 6.20. The differential Yap correction has a small effect on the Nusselt number predictions of the free-disc flow (see Figure 6.21), whereas the "standard" Yap correction returns results practically identical to those obtained using the same model without the Yap correction.

In addition to the above comments on the need for the Craft *et al*. modifications, it was found necessary to activate the differential length-scale correction only once the calculated flow field had settled down and the boundary layer had partially developed. Introducing the differential Yap correction at the start of a calculation led to divergence due to fluctuations in the turbulence length scale.

6.3.7 Code Validation

To show that the code used in the present study produced the correct behaviour in the laminar region of the free-disc flow, the flow up to a rotational Reynolds number of $100,000$ was studied using the same low-Reynolds-number model employed in turbulent flow calculations. Following a similar study undertaken by Kiliç [128], the height of the domain was set to $0.03D$ (where D is the disc diameter) which corresponded to at least three times the boundary layer thickness predicted by Cochran's numerical solution of von Kármán's equations for laminar flow over the free-disc [131]. Calculations

specified in addition to values of k and $\tilde{\varepsilon}$.

were performed on a 60×60 grid (shown in Figure 6.22) with the Launder & Sharma $k-\varepsilon$ model [13].

Figure 6.23 shows the three velocity components in dimensionless form, as suggested by von Kármán [129], compared to the similarity solutions of Owen & Rogers [132]. Symbols show the result of overlaying the predicted velocity at three different Reynolds numbers, $Re_\phi = 9000$, 25000 and 49000. The three results at different Reynolds numbers are indistinguishable and show excellent agreement with the calculations of Owen & Rogers. The predicted moment coefficient, c_m, defined as the dimensionless integral moment on the disc ($c_m = M/0.5\rho\Omega^2 r^5$, where $M = -2\pi \int_0^r r^2 \tau_\phi \mathrm{d}r$), is shown in Figure 6.24. At the outer edge of the disc, the low-*Re* model agreed with Cochran's [131] solution for c_m to within 6 significant figures. However, there is a greater discrepancy between the present predictions and Cochran's values as one approaches the axis of the disc where, at $Re_\phi = 6000$, there is a difference of 15%. This discrepancy may simply be due to any errors in the numerical integration used to calculate the moment coefficient increasing as the radial width of the cell, Δr, increases relative to the radial position, r. These results were considered to show satisfactory validation of the numerical code performance, at least at low Reynolds number.

6.4 Calculated Flow Results

6.4.1 Linear $k-\varepsilon$ Model

Figures 6.25 – 6.28 compare the radial and tangential velocity profiles obtained using the three standard wall functions and the new UMIST-*N* wall function at three radial positions with results obtained from the low-Reynolds-number Launder & Sharma model and the experimental velocity measurements by Cham & Head [116]. In these figures, the distance from the wall, y, is non-dimensionalized with the momentum thickness, $\theta = \int_0^\infty |W/\Omega r\,(1 - W/\Omega r)|\,\mathrm{d}y$. Semi-logarithmic plots of the dimensionless radial and tangential velocity[8], U^* and W^*, are also shown for the different wall functions and compared to the low-*Re* predictions and the "universal" log-law in Figures 6.29 – 6.32. Radial and tangential wall shear stress predictions for the four different wall functions are presented in Figures 6.33 – 6.40, where results using four different main-grid arrangements are compared to low-*Re* model predictions. Similarly, integral and local values of the Nusselt number are presented for the different wall treatments and grid arrangements in Figures 6.41 – 6.49. Although integral Nusselt number comparisons are informative, since experimental data is available (Cobb & Saunders [130]), the integral Nusselt number involves averaging the heat transfer across the whole of the disc and therefore the transition from laminar to turbulent flow is indistinct. To enable a closer examination of transition, plots of the local Nusselt number are also provided. Finally, the y^+ values for the different main-grid arrangements are shown in Figures 6.50 – 6.53.

All of the wall functions show good agreement with the low-*Re* tangential velocity profiles as one

[8]The superscript $*$ refers to the velocity scaling used by Chieng & Launder [49], where $U^* = k^{1/2}U/\left(\tau_{wall,r}/\rho\right)$ and $y^* = k^{1/2}y/\nu$ (i.e. $U^+ = c_\mu^{1/4}U^*$ and $y^+ = c_\mu^{1/4}y^*$) and the local value of k is used, not the value at the near-wall node.

might expect, since the tangential velocity exhibits a log-law profile in the fully-turbulent inner-region of the boundary layer. The radial velocity is under-predicted by both the SCL and the CL treatments (Figures 6.26 and 6.27) but the TEAM wall function, which assumes a fully-turbulent boundary layer across the whole of the disc, shows surprisingly good agreement with the radial velocity predicted by the low-*Re* model (Figure 6.25). However, Figures 6.29, 6.30 and 6.31 show that the logarithmic profile is clearly inapplicable for the radial velocity. Similarly, the wall shear stress predicted by the standard wall functions (Figures 6.33 – 6.38) shows good agreement with the low-*Re* model in the tangential direction but poor agreement with the radial wall shear stress. Here, the use of the log-law to prescribe the radial velocity results in the underprediction of the low-*Re* model radial wall shear stress by up to 50%. Moreover, the TEAM, SCL and CL wall functions all exhibit a strong sensitivity in the predicted radial wall shear stress to the size of the near-wall cell (as indicated by the grid size in Figures 6.34, 6.36 and 6.38).

The predicted velocity using the UMIST-*N* wall function shows excellent agreement with the low-*Re* model results on both linear and semi-log axes (Figures 6.28 and 6.32 respectively). The velocity predictions also show good agreement with the experimental profiles although the near-wall peak in the radial velocity is under-predicted slightly at $Re_\phi = 1 \times 10^6$ and $Re_\phi = 2 \times 10^6$. The main-grid values of the tangential velocity, W^*, are slightly higher than the low-*Re* model predictions shown in Figure 6.32. This may be due to the linear interpolation used to define the boundary conditions at the outer edge of the subgrid. A similar small discrepancy in the log-law was found in the fully-developed channel flow between the near-wall main-grid nodal values and the low-*Re* result. In contrast to the standard wall function predictions, the wall shear stress in both the radial and tangential directions predicted by the UMIST-*N* wall function is in good agreement with the low-*Re* model predictions (Figures 6.39 and 6.40). The UMIST-*N* results also show far less sensitivity to the size of the near-wall cell than the other wall functions. The coarsest main-grid mesh with 22×120 cells gave somewhat lower tangential wall shear stress and slightly higher radial wall shear stress than that predicted by the low-*Re* model and the other UMIST-*N* wall-function grids. The number of subgrid nodes across the wall-adjacent control volume with the 22×120 grid was sufficient to give results independent of the subgrid node density and therefore the disparity between this result and the other UMIST-*N* wall function results must be due to the relative coarseness of the main-grid. In fact, as shown in Figure 6.53, the maximum y^+ with the 22×120 grid was over 300, which is more than three times the recommended maximum cell size suggested by Morse [124] and Virr *et al*. [121] for the spinning free-disc flow.

At rotational Reynolds number, Re_ϕ, above $20,000$ the predicted local Nusselt number using the TEAM wall function (Figure 6.42) increases linearly with rotational Reynolds number and misses altogether the transition from laminar to turbulent flow predicted by the low-Reynolds-number model and observed experimentally. The TEAM wall function exhibits little dependence upon the size of the near-wall cell at high-Re_ϕ. However, at low rotational Reynolds number ($Re_\phi < 20000$) the predicted Nusselt number is sensitive to the grid size, as shown by the integral Nusselt number plot (Figure

6.41). Near the axis of the disc, at low-Re_ϕ, the wall-adjacent node is located within the viscous sublayer and hence a linear velocity profile is assumed. However, since the wall-function grid does not contain sufficient nodes to resolve the near-wall flow, the solution is grid-dependent. The Nusselt number predicted with the SCL and CL wall functions is even more sensitive to the size of the near-wall cell (Figures 6.43 and 6.45). Additionally, the SCL and CL treatments produced spikes in the local Nu profile near transition due to the switch used to select laminar or turbulent wall functions at a specified y^+. As previously noted (see Section 6.3.5) these results are dependent upon the initial turbulence levels chosen.

The UMIST-*N* wall function shows good overall agreement with the low-*Re* Nusselt number (Figures 6.47 and 6.48). The slope of the Nu profile in the laminar and turbulent regions of the flow are close to those observed with the low-*Re* model but there is some sensitivity to the size of the near-wall cell in the predicted transition location. Using different near-wall cell sizes corresponding to maximum y^+ between 70 and 310, the transition point varied from $Re_\phi \approx 0.7 \times 10^5$ to $Re_\phi \approx 2.1 \times 10^5$, whereas the low-*Re* model predicted transition at $Re_\phi \approx 1.2 \times 10^5$. Although this feature is undesirable, it is not entirely surprising since it is well known that the correct prediction of transition is highly sensitive to the numerical scheme. It was shown earlier that transition is sensitive to radial grid density and the use of logarithmic coordinates in Figures 6.47 and 6.48 also magnifies any small differences in the location of transition. The same results to those shown in Figure 6.48 are plotted on linear axes in Figure 6.49 which shows that the local Nusselt number predicted using the coarsest main-grid mesh of 22×120 cells is somewhat lower than that predicted by the finer grids, a consequence of the poor resolution of the flow with so few main-grid nodes.

6.4.2 NLEVM

Figure 6.54 compares the predicted integral and local Nusselt number for the free-disc flow using the low-Reynolds-number linear and non-linear $k-\varepsilon$ models. There is little difference in the heat transfer predictions between the two models with the exception that the NLEVM delays slightly the onset of transition compared to the linear model, from $Re_\phi = 115,000$ to $150,000$. The similarity between the two different models is not entirely unexpected, since the additional terms in the NLEVM are primarily effective in cases of separation and impingement (features which are absent from the spinning free-disc flow). Radial and tangential velocity profiles for the linear and non-linear models are shown in Figure 6.55 and semi-logarithmic U^* and W^* profiles are shown in Figure 6.56. In each case, profiles are shown for three radial positions, corresponding to the rotational Reynolds numbers at which Cham & Head [116] obtained experimental velocity measurements. The two models are practically indistinguishable on the linear axes velocity plots whilst the NLEVM predicts a slightly higher value of U^* and W^* in the fully-turbulent region ($20 \leq y^* \leq 200$). This latter effect was due to a difference in the near-wall turbulent kinetic energy profile predicted by the two models. Figures 6.57 and 6.58 compare normal and shear Reynolds stress profiles at three different rotational Reynolds numbers obtained using the low-*Re* linear $k-\varepsilon$ model and the NLEVM (unfortunately no experimental

data has been found with which comparisons can be drawn). As expected, the linear model produces an isotropic stress field ($\overline{u^2} \approx \overline{v^2} \approx \overline{w^2}$) whilst, with the NLEVM, the tangential component of the normal stress $\left(\overline{w^2}\right)$ is significantly higher than the axial and radial components ($\overline{u^2}$ and $\overline{v^2}$). The shear stresses in planes normal to the wall ($\overline{uv}$ and $\overline{vw}$) are practically identical with the linear and non-linear models. The most striking feature of the Reynolds stress profiles is with the shear stress in the plane parallel to the wall ($\overline{uw}$). The linear $k-\varepsilon$ model predicts this to be practically zero whilst the NLEVM predicts a comparatively large and negative near-wall value that increases towards a positive peak at $y/\theta = 4$ and then decays towards the edge of the boundary layer. In a linear model, the $\overline{uw}$ shear stress is calculated from:

$$-\rho\overline{uw} = \mu_t r \frac{\partial}{\partial r}\left(\frac{W}{r}\right) = \mu_t\left(\frac{\partial W}{\partial r} - \frac{W}{r}\right) \tag{6.5}$$

The wall velocity is a linear function of the radius (i.e. $W_{wall} = \Omega r$) so near the wall at least one would expect $\partial/\partial r\,(W/r) = 0$. Figure 6.59 shows the velocity profiles at three radial positions, also shown in Figure 6.55, overlaid on the same set of axes. The dimensionless tangential velocity $(W/\Omega r)$ shows little change between a rotational Reynolds number of 3.4×10^5 and 2×10^6. The negligible value of $\overline{uw}$ predicted by the linear model is thus a consequence of the radial gradient of (W/r) being close to zero. The shear stress $\overline{uw}$ is not zero with the non-linear $k-\varepsilon$ model since the stress is also affected by quadratic and cubic functions of strain-rate and vorticity.

Previous studies have shown that the Craft *et al*. two-equation NLEVM can produce unrealizable (negative) axial normal stress, $\overline{v^2}$, in flows where there is a strong swirling component of velocity [133]. In a purely swirling flow, the only velocity gradient is $\partial W/\partial r$ and hence the only finite vorticity component is $\Omega_{13} = -\partial W/\partial r - W/r$. Simplifying the expression for turbulence anisotropy, Equation (2.27), the axial normal stress is given by:

$$\overline{v^2} = \frac{2}{3}k - \frac{2}{3}c_3\frac{\nu_t k}{\tilde{\varepsilon}}\left(\Omega_{13}\right)^2 \tag{6.6}$$

The sign of $\overline{v^2}$ is thus dependent upon the value of the constant c_3 which the Craft *et al*. non-linear $k-\varepsilon$ model takes as $c_3 = 0.26$. Gatski & Speziale [27] recommended that coefficient of the quadratic vorticity term (which, in the Craft *et al*. model corresponds to c_3) should be zero in purely swirling flow. The three-equation $k-\varepsilon-A_2$ model Craft *et al.* [134] used invariants of the strain-rate and vorticity tensors to remove the non-linear contribution to $\overline{v^2}$ in purely swirling flow. The free-disc flow is not a purely swirling flow, having significant velocity gradients in the axial (wall-normal) direction and finite radial velocity. In the present study it was found that, using the Craft *et al.* $k-\varepsilon$ model, the normal stress was positive near the wall, as shown in Figure 6.57. Away from the wall, towards the edge of the turbulent boundary layer, the normal stress decreased to zero and in some cases there were small overshoots with negative normal stress levels of approximately -10^{-14}. Since the gradient of the stress is used in the momentum equations, rather than its actual value, the small negative stresses were inconsequential.

Figures 6.60 – 6.63 compare the predicted velocity using four different wall functions with the

low-*Re* NLEVM results and experimental data from Cham & Head [116]. Semi-logarithmic plots of the dimensionless velocity, U^* and W^*, are shown for the different wall functions and compared to the low-*Re* predictions and the "universal" log-law in Figures 6.64 – 6.67. Predicted integral Nusselt number are also shown for the four different wall functions and compared to the low-*Re* NLEVM result and experimental data from Cobb & Saunders [130] in Figures 6.68 – 6.71. The behaviour of the wall functions with the NLEVM is practically identical to that previously observed with the linear $k-\varepsilon$ model (see above). The UMIST-*N* wall function shows superior performance to the other wall functions in predicting the radial and tangential velocity in the fully-turbulent region of the boundary layer and the location of transition predicted by the UMIST-*N* wall function shows a similar degree of dependence upon the size of the near-wall cell to that exhibited by linear model.

6.5 Computational Costs

Tables 6.4 and 6.5 show comparisons of computing times for the free-disc flow using the linear and non-linear $k-\varepsilon$ turbulence models respectively. In all cases the turbulence field was initialized with $k = 10^{-5}(\Omega r)^2$ and $\mu_t = 10\mu$. Under-relaxation factors used in the low-*Re* and standard wall-function calculations and in the main-grid region of the UMIST-*N* wall-function calculations are those given in Section 6.3.2. The QUICK differencing scheme was used for momentum and temperature equations (except for the wall-adjacent cells) and PLDS was used for all other quantities. Calculations were performed on a single processor of a Silicon Graphics *Origin 2000* with the same levels of compiler optimization in each case. The UMIST-*N* wall function required 30 subgrid cells in order to obtain grid-independence.

Model Tested	No. of Nodes	Time per Iter (*s*)	No. of Iterations	Total CPU Time (*s*)	Relative CPU Time
TEAM WF	120×28	0.07	2009	136	1
Chieng & Launder	120×28	0.07	2208	154	1.1
UMIST-*N*	$120 \times 28(+30)$	0.14	2363	339	2.2
Low-*Re*	120×70	0.20	19928	3996	29.4

Table 6.4: Computing times for the free-disc ($Re = 3.3 \times 10^6$) with the linear $k-\varepsilon$ model

Model Tested	No. of Nodes	Time per Iter (*s*)	No. of Iterations	Total CPU Time (*s*)	Relative CPU Time
TEAM WF	120×28	0.11	3917	410	1
Chieng & Launder	120×28	0.10	4181	415	1.0
UMIST-*N*	$120 \times 28(+30)$	0.19	3623	692	1.7
Low-*Re*	120×70	0.25	21390	5272	12.9

Table 6.5: Computing times for the free-disc ($Re = 3.3 \times 10^6$) with the non-linear $k-\varepsilon$ model

In the previous study of an impinging jet using different wall treatments (Chapter 5), the UMIST-*N*

wall function was up to 60% slower than the Chieng & Launder wall function and about 8 times faster than a low-Reynolds-number model. In the present study, with the linear $k-\varepsilon$ model, the UMIST-*N* wall function takes twice as long as a standard wall function but is more than 13 times faster than the low-*Re* model. Using the NLEVM, the difference is slightly less with the UMIST-*N* wall function taking 70% more computing time than the Chieng & Launder wall function but only one eighth of that of the low-Reynolds-number model.

There are several factors which increase the relative computing times for the free-disc flow. Firstly, there are two wall-parallel velocity components in the free-disc flow, whereas the axisymmetric impinging jet tested previously did not have a swirling velocity component. The swirling and radial components of velocity are also strongly coupled in the free-disc flow through the source terms appearing in the U and W momentum equations. The number of nodes in the wall-parallel direction used in the present calculations exceeds that used in the earlier study and if one multiplies the number of transport equations solved per-node by the number of nodes for the impinging jet and the free-disc, one finds that in the impinging jet the number of calculations performed in a low-*Re* iteration was twice that of the standard wall functions whilst in the free-disc the corresponding ratio was 2.5.

6.6 Discussion & Conclusions

It has been shown that “standard” wall-functions have a number of shortcomings in predicting the free-disc flow. The “universal” log-law adequately approximates the near-wall tangential velocity profile but is inappropriate for the radial velocity. Moreover, standard wall functions are unable to account correctly for transition from laminar to turbulent flow. It has been demonstrated that new UMIST-*N* wall-function treatment, based on the integration of simplified transport equations across a near-wall subgrid, is able to capture the skewing of the velocity profile in the near-wall region and shows excellent agreement with velocity predictions obtained using low-Reynolds-number treatments. Nusselt number predictions using the UMIST-*N* wall function are also in good agreement with those of low-*Re* models in contrast to the other standard wall functions tested. The location of transition from laminar to turbulent flow predicted by the UMIST-*N* wall function showed some sensitivity to the size of the near-wall control volume although the results were close to those obtained with low-*Re* models. The UMIST-*N* wall function calculation was also between 8 and 13 times faster than the corresponding low-Reynolds-number calculation in the free-disc flow, similar to the savings observed previously in an impinging jet flow.

The linear $k-\varepsilon$ model of Launder & Sharma [13] and the non-linear $k-\varepsilon$ model of Craft *et al*. [67] were both tested. Results with the two models were broadly similar except for a slight delay in transition with the NLEVM and some differences with the stress profiles. It was found that the more recent Craft *et al*. [67] version of the differential length scale correction was necessary in the free-disc flow calculations to prevent numerical instability arising from significant turbulence length scale gradients at the outer edge of the turbulent boundary layer.

During the course of the present study, some interesting features relating to the initialization of free-disc flow calculations were investigated. "Natural" transition was obtained in the computational model by initializing the flow domain with a uniform level of turbulence; as the calculation progressed, turbulence decayed in regions of low strain-rate leaving a laminar boundary layer near the axis of the disc whilst at higher rotational Reynolds number the boundary layer remained turbulent. However, it was found that the onset of transition from laminar to turbulent flow could be shifted by starting the calculation from a different "guessed" turbulence level. One could even completely laminarize the boundary layer by starting a low-*Re* calculation with relatively low, but finite turbulence levels ($\mu_t = 10\mu$ and $k = 10^{-5}\left(\Omega r_b\right)^2$). This sensitivity to the initial turbulence level was traced to the near-wall turbulence damping terms which, during the initial stages of the calculation, were of considerable magnitude due to the large velocity gradient between the spinning wall and nearby cells. It was found that by freezing the eddy-viscosity and solving initially only the mean-flow equations (i.e. momentum equations and pressure-correction) before commencing the solution of the turbulence parameters, one could obtain low-*Re* model predictions that were independent of the initial turbulence levels. This finding was used retrospectively to explain previous studies of the free-disc flow where, for example, Kiliç [128] was able to capture natural transition (by using a multigrid solver where k and ε were only solved on the finest grid) whilst Morse [126] was forced to apply an *ad hoc* correction to the eddy-viscosity in order to obtain transition.